Concept, modeling, and performance prediction of a low-cost, large deformable mirror

Heimsten, Rikard; MacMynowski, Douglas G.; Andersen, Torben; Owner-Petersen, Mette

Published in:
Applied Optics

DOI:
10.1364/AO.51.000515

2012

Citation for published version (APA):
Heimsten, R., MacMynowski, D. G., Andersen, T., & Owner-Petersen, M. (2012). Concept, modeling, and performance prediction of a low-cost, large deformable mirror. *Applied Optics*, *51*(5), 515-524. https://doi.org/10.1364/AO.51.000515

Total number of authors:
4

LUND UNIVERSITY

PO Box 117
221 00 Lund
+46 46-222 00 00

Concept, modeling, and performance prediction of a low-cost, large deformable mirror

Rikard Heimsten,[1,*] Douglas G. MacMynowski,[2]
Torben Andersen,[1] and Mette Owner-Petersen[1]

[1]Lund Observatory, Lund University Box 43, SE-221 00 Lund, Sweden

[2]Control and Dynamical Systems, California Institute of Technology,
1200 E. California Blvd., Pasadena, California 91125, USA

*Corresponding author: rikard.heimsten@telia.com

Received 18 August 2011; revised 1 November 2011; accepted 2 November 2011;
posted 2 November 2011 (Doc. ID 153084); published 2 February 2012

While it is attractive to integrate a deformable mirror (DM) for adaptive optics (AO) into the telescope itself rather than using relay optics within an instrument, the resulting large DM can be expensive, particularly for extremely large telescopes. A low-cost approach for building a large DM is to use voice-coil actuators connected to the back of the DM through suction cups. Use of such inexpensive voice-coil actuators leads to a poorly damped system with many structural modes within the desired bandwidth. Control of the mirror dynamics using electro-mechanical sensors is thus required for integration within an AO system. We introduce a distributed control approach, and we show that the "inner" back sensor control loop does not need to function at low frequencies, leading to significant cost reduction for the sensors. Incorporating realistic models of low-cost actuators and sensors together with an atmospheric seeing model, we demonstrate that the low-cost mirror strategy is feasible within a closed-loop AO system. © 2012 Optical Society of America

OCIS codes: 010.1285, 010.1330, 080.4035, 220.1080, 220.4830.

1. Introduction

Most modern ground-based optical telescopes use adaptive optics (AO) with one or more deformable mirrors (DMs) for correction of atmospheric disturbances. It is useful to include large DMs in a telescope system to avoid lossy relay optics and to make the telescope more compact [1]. Large DMs typically have either piezo-electrical (displacement) or voice-coil (force) actuators. For example, a concept including piezo-electrical actuators has been proposed for the E-ELT [2] and the 911 mm-diameter deformable secondary mirrors for the large binocular telescope AO system using a concept encompassing force actuators, applied by an Italian group based at the Arcetri Astrophysical Observatory. The project team first demonstrated correct function of the DM in a laboratory environment [3], and first light on the telescope was made in 2010 [4].

Potential low-cost voice-coil actuators and position sensors have been described in [5] and are shown in Fig. 1. The actuators encompass a moving rod, which is driven by a voice coil and has a linear variable differential transformer (LVDT) measuring the relative position of the rod. Use of commercially available voice coils, which limit the actuator bandwidth compared to the force actuators used in [3,4], can reduce the costs. The rod is connected to the DM through a suction cup, avoiding direct physical contact between the mirror and the actuators. Internal feedback loops in the actuators increase the bandwidth of the actuators. A system with such actuators can be inexpensive because tight tolerances are not needed. As a comparison, the existing force actuators used for large DMs [3,4] use permanent magnets glued to

1559-128X/12/050515-10$15.00/0

the back of the mirror, which give a large uniform (flat) frequency response. In contrast, the actuator concept proposed here has a flat response of only a few kHz, and there is no need for extra components at the back of the mirror. Low-cost back sensors to measure mirror deflection can be made using electret microphones in rubber bellows. However, these sensors do not respond statically, nor is it straightforward to collocate them with the actuators.

A distributed control approach for a thin mirror using force actuators was introduced in [6]. The control system includes rate feedback (adding damping) and position feedback (adding stiffness), similar to [7]. However, [6] introduces two key elements: the theory needed to understand rate feedback design constraints associated with finite bandwidth, allowing for sensors that are not exactly collocated with the actuators, and a robust local control scheme involving actuator families that suppresses coupling between adjacent actuators to reduce excitation of low-order eigenmodes [8]. This local approach is more robust than a global approach, because it does not rely on an accurate model.

We introduce in this paper a DM concept, which has the potential of being much cheaper than other proposed DM concepts, using the actuator and sensor concepts mentioned above, and demonstrate that it is feasible within an AO system. Electro-mechanical feedback from sensors is used to compensate for the mirror dynamics using distributed control as in [6]. We show that performance within an AO system does not require sensor static information, nor does it require actuator/sensor collocation. We use a finite element model of a test mirror as an example, and real actuator and sensor characteristics, and incorporate such a DM into a simulation of an AO system on a practical telescope. Working in both the temporal and frequency domains, we demonstrate that the mirror will fulfill the requirements for being part of an AO system.

2. Deformable Mirror

The DM concept is shown in Fig. 1. There are voice-coil actuators in a regular pattern on the back of the mirror to deform the mirror into the correct form. The back sensors are located between the actuators and operate in a frequency range of 20–5000 Hz. In a closed-loop AO system, there is also a wavefront sensor (WFS) measuring the form of the mirror from DC up to a frequency determined by the sampling frequency of the WFS (typically 500 Hz).

The combination of force actuators and a thin mirror leads to a poorly damped system with many structural resonances within the desired bandwidth of the AO system. The main challenge of such a system is to establish a stable control strategy with a high bandwidth. In control terminology, the DM is the "plant" for the AO control system.

A typical closed-loop AO bandwidth is roughly 50 Hz, so the DM must respond to actuator commands with a relatively flat response and a small phase lag up to that frequency. However, as shown in Fig. 2, the faceplate transfer function has many resonances and antiresonances within that frequency range. The control strategy includes rate and position feedback, adding damping and stiffness, further discussed in Subsection 2.C.

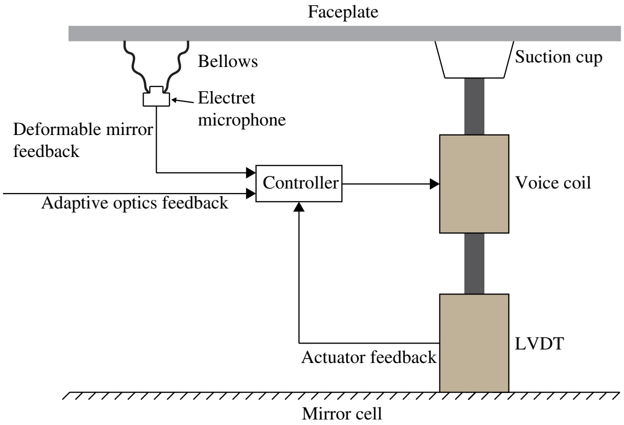

Fig. 1. (Color online) Conceptual design of force actuators and position sensors. The controller is dependent on information from the three sensor feedback loops.

A. Faceplate

For a case study, we use a 2 mm thick, 1 m diameter flat faceplate fixed at the inner rim. It is made of borosilicate with the material data given in Table 1. A finite element model of the faceplate was set up with the software package "Comsol Multiphysics." For a near-infrared operation wavelength, the actuator pitch should be 70 mm or less for the sagging effects (due to gravity) between two support points to be neglected. Here we chose to have 372 actuators placed in a square topology with an actuator pitch of 45 mm, as shown in Fig. 3. This is the smallest achievable actuator pitch with the current actuator design. The optical reason for choosing a 45 mm pitch is given in Section 4. The 702 back sensor nodes are each located between two adjacent actuators; i.e., each actuator in general has four neighboring sensors. In addition to the actuator and sensor nodes,

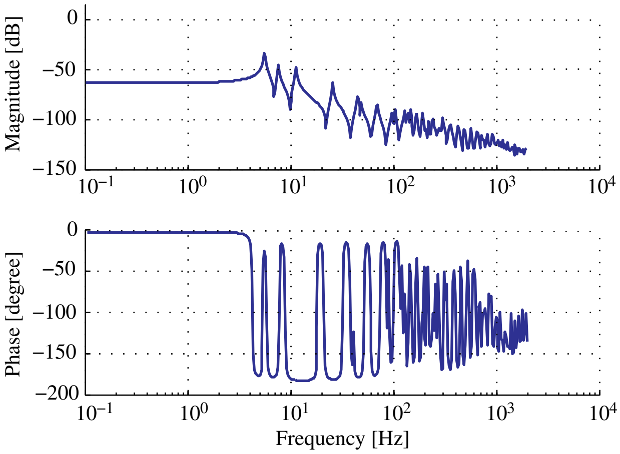

Fig. 2. (Color online) Transfer function of the DM from force to position (average of four neighboring sensors) at the same location.

Table 1. Nomenclature and Parameter Values for a 1 m DM Used for Performance Studies

Parameter	Definition	Value
E	Young's modulus	63×10^9 Pa
ρ	density	2.23×10^3 kg/m^3
ν	Poisson ratio	0.2
h	DM thickness	2 mm
D	bending stiffness	$Eh^3/12(1-\nu^2)$
r	radius of the mirror	0.5 m
A	DM area	πr^2
ζ	damping ratio	1%

another 4000 nodes are used in the finite element model.

The dynamic behavior of the faceplate is described by the differential equation

$$\mathbf{M}\frac{d^2\boldsymbol{\xi}}{dt^2} + \mathbf{E}\frac{d\boldsymbol{\xi}}{dt} + \mathbf{K}\boldsymbol{\xi} = \mathbf{f},$$

where **M**, **E**, and **K** are, respectively, the mass, damping, and stiffness matrices, **f** is a force vector, and $\boldsymbol{\xi}$ is a vector of angular and translational displacements. The first eigenfrequency is at 5.6 Hz, and there are another 12 eigenfrequencies below 50 Hz, i.e., within the expected bandwidth for an AO system.

Guyan reduction and modal truncation were used to obtain a more computationally practical model. Guyan reduction reduced the number of degrees of freedom for each node to three, retaining out-of-plane translation and the two rotations around the in-plane axes. Modal truncation removed the modes with eigenfrequencies above 10 kHz. Mode acceleration was applied to include the static contribution from the modes omitted by the truncation.

Structural performance of the faceplate, represented by the transfer function from force to position at one location as shown in Fig. 2, can be understood from a wave-based description. Resonances arise due to constructive interference of the bending waves reflecting off the faceplate boundaries. Above a certain frequency, the response is no longer dominated by sharp resonance and antiresonance peaks, because many different modes overlap. The transition to this "acoustic" region begins where the half-power bandwidth of a mode exceeds the average modal spacing by a factor of 2 or 3, at a frequency [6] of

$$f_{\mathrm{ac}} = 2\sqrt{\frac{D}{\rho h}\frac{1}{A\zeta}}, \tag{1}$$

where the nomenclature is defined in Table 1. For example, for a DM of borosilicate with a diameter of 1 m and a thickness of 2 mm, the transition frequency is about 1300 Hz.

Use of a noncollocated sensor and actuator scheme gives rise to phase lag, which is tolerable as long as the distance between the actuators and sensors is no more than [6]

$$d < \frac{c_{\mathrm{B}}}{8 f_{\mathrm{ac}}},$$

where c_{B} is the bending wave speed in the plate, and f_{ac} is given by Eq. (1).

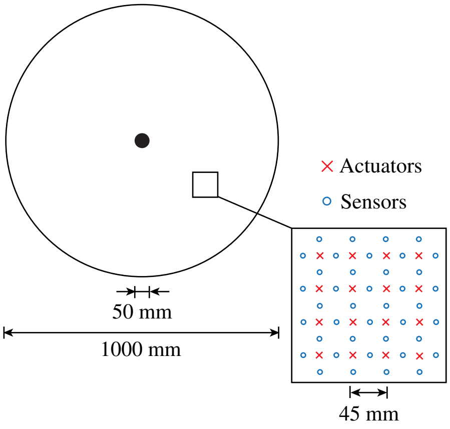

Fig. 3. (Color online) The topology of the actuator and sensor positions for the 1 m case study.

B. Actuators and Sensors

The dynamical behavior of the actuators and the sensors can be represented by state-space models. The equation of motion for an actuator in the Laplace domain is given by

$$F = (ms^2 + es + k)\delta_{\mathrm{r}},$$

where m is the mass and δ_{r} is the position of the moving rod, and F is the electromagnetic force developed by the voice coil, which is the product of its force constant and the current in the winding. The suction cup can be viewed as a spring with stiffness k and damping coefficient e. A local current loop can be added to suppress the influence of the inductance and the back electromotive force of the voice coil. Thus, we can assume that the current is proportional to an input voltage, U, and the transfer function from voltage to rod displacement is

$$\frac{\delta_{\mathrm{r}}}{U} = \frac{C}{ms^2 + es + gC + k}, \tag{2}$$

where g is the proportional gain of the local feedback loop from the LVDT and C is a design dependent constant. The natural frequency, ω_{a}, and the damping, ζ_{a}, of the second-order system in Eq. (2) is

$$\omega_{\mathrm{a}} = \sqrt{\frac{gC + k}{m}},$$
$$\zeta_{\mathrm{a}} = \frac{e}{2\sqrt{m(gC + k)}}.$$

Choosing appropriate scaling, we can let $C = 1$. A state-space realization of Eq. (2) is given by

$$\mathbf{A}_\mathrm{a} = \begin{bmatrix} -2\zeta_\mathrm{a}\omega_\mathrm{a} & -\omega_\mathrm{a}^2 \\ 1 & 0 \end{bmatrix},$$

$$\mathbf{B}_\mathrm{a} = \begin{bmatrix} \omega_\mathrm{a}^2 \\ 0 \end{bmatrix},$$

$$\mathbf{C}_\mathrm{a} = [0 \quad 1],$$

$$\mathbf{D}_\mathrm{a} = 0.$$

The sensors on the back of the mirror, shown in Fig. 1, encompass electret microphones inside bellows. Such a sensor can be viewed as a pressure sensor with a flat region of the frequency response between the low-pass cutoff, ω_lp, and the high-pass cutoff, ω_hp. The transfer function is given by

$$H_\mathrm{sen}(s) = \frac{s}{s + \omega_\mathrm{hp}} \cdot \frac{\omega_\mathrm{lp}}{s + \omega_\mathrm{lp}}.$$

Here, we neglect scaling factors. The equation can be converted to state-space form:

$$\mathbf{A}_\mathrm{s} = \begin{bmatrix} 0 & -\omega_\mathrm{hp}\omega_\mathrm{lp} \\ 1 & -\omega_\mathrm{hp} - \omega_\mathrm{lp} \end{bmatrix},$$

$$\mathbf{B}_\mathrm{s} = \begin{bmatrix} 0 \\ \omega_\mathrm{lp} \end{bmatrix},$$

$$\mathbf{C}_\mathrm{s} = [0 \quad 1],$$

$$\mathbf{D}_\mathrm{s} = 0.$$

The corner frequencies are 20 Hz and 5 kHz for our design [5].

The electret microphones can detect a pressure change, Δp, of around 0.2 Pa. The corresponding volume change is computed from

$$\Delta v = -\frac{v\Delta p}{1.4p},$$

obtained by differentiation of the state equation for an adiabatic ideal gas, where p is the internal pressure in the bellows. Assuming no dynamics in the bellows between the corner frequencies, the volume change is proportional to the deflection of the mirror. With the dimensions chosen, the electret microphones can sense a deflection of about 10 nm.

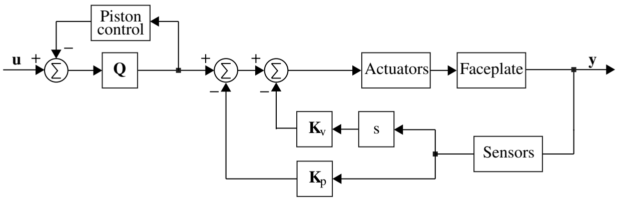

Fig. 4. Block diagram of the DM system. The actuator, faceplate, and sensor modules represent the state-space models derived in Subsections 2.A and 2.B. The input **u** is the commanded displacement.

C. Faceplate Control

The DM system is shown in Fig. 4. The three blocks "Actuators," "Faceplate," and "Sensors" represent the state-space models for these mechanical parts. The gains of the position and rate feedback loops are represented by the diagonal matrices $\mathbf{K}_\mathrm{p}$ and $\mathbf{K}_\mathrm{v}$, respectively. A differentiator is used for the rate feedback, since the electret microphones are position sensors. The piston control is required to reduce excessive stresses at the attachment points of the faceplate.

A force command to one actuator produces a global response, similar to the tip/tilt mode, for the whole mirror. The loop gain of the faceplate is about 30 times higher for low spatial than for high spatial frequencies. The substantial coupling between actuators is reduced by the matrix $\mathbf{Q}$, shown in Fig. 4. It is in principle possible to obtain $\mathbf{Q}$ by inverting the faceplate model, but the system may not be robust if the plant is not modeled with high accuracy [6]. We instead propose a local scheme, using a set of actuator families, each centered on an actuator. A desired displacement command (input to $\mathbf{Q}$ in Fig. 4) at a particular actuator location results in a force distribution applied to all the actuators in that family. The force distribution in each family is determined by minimizing the cost function

$$J = \|\mathbf{K}_\mathrm{a}^{-1}\mathbf{f} - \boldsymbol{\xi}\|, \tag{3}$$

where $\mathbf{f}$ is the force vector for the actuator nodes, and $\boldsymbol{\xi}$ is a vector defining the desired displacements at the actuator nodes, defined below. A static condensation of the full stiffness matrix is used to form $\mathbf{K}_\mathrm{a}$, which then only retains the out-of-plane translation degrees of freedom for the actuator nodes. The elements of the force vector $\mathbf{f}$ in Eq. (3) are constrained to be

$$f_i = 0 \quad \text{for } i \notin \text{family}, f_i \in \mathbb{R} \quad \text{for } i \in \text{ ,family}$$

where i is the actuator number. The elements of the displacement vector, $\boldsymbol{\xi}$, for a family centered on the j-th actuator are

$$\xi_i = 0 \quad \text{for } i \neq j, \xi_i = 1 \quad \text{for } i = j.$$

Using this approach, the computed force vectors for each family are stored as columns in the family matrix $\mathbf{Q}$. Each column corresponds to a command vector for a specific center actuator. We have chosen a family size with two rings of actuators around the centered actuator, in total 21 actuators. We note that the family concept will not work satisfactorily with very closely located actuators, because the corresponding forces become excessive. In fact, this not only applies to our concept but also is related to the flexibility of the mirror.

A comparison between use of a single actuator and a family centered on the same actuator can be made by studying the influence functions for the two cases. The influence function for a single actuator is largely dominated by a tip/tilt shape (the lowest frequency, most compliant mode of the faceplate), whereas the influence function for the family is essentially a local deformation at the center actuator of the family.

To further demonstrate the properties of the control system with the family concept, we use the faceplate model introduced in Subsection 2.A as an example. In this study, piston control is not included. To study the dynamical behavior of the system, we compute frequency responses for two cases:

- Case 1: The input command vector, $\mathbf{u}$, of Fig. 4 is a pure tip and its magnitude at a representative location is taken as scalar input, and the output is the displacement measured at the same location. The objective is to study low spatial frequency behavior.
- Case 2: The input command vector, $\mathbf{u}$, has all zeros except at a representative location. The magnitude of the input at that location is then the scalar input, and the output is the displacement at the same location. The objective is to study high spatial frequency behavior.

The frequency response of the mirror alone, i.e., when $\mathbf{K}_\mathrm{v}$ and $\mathbf{K}_\mathrm{p}$ of Fig. 4 are null matrices and $\mathbf{Q}$ an identity matrix, is shown as solid curves in Fig. 5. As expected, the first eigenfrequency at 5.6 Hz corresponds to the tip/tilt mode and is seen both for Cases 1 and 2. Closing the rate feedback loops with a diagonal $\mathbf{K}_v$ matrix and ideal sensors gives the dashed lines in Fig. 5. The system is overdamped at lower frequencies for the gain needed to damp eigenfrequencies up to the acoustic frequency. With nonideal sensors, there is hardly any overdamping, since their response drops off below 20 Hz. The transfer function of the system with closed rate feedback and nonideal sensors is shown as dotted curves in Fig. 5.

Including the family matrix, $\mathbf{Q}$, in the control system has two effects. Besides decoupling adjacent actuators from each other, eigenmodes with eigenfrequencies below 30 Hz are much less excited by input commands when $\mathbf{Q}$ is included. The second effect is important since the low-order eigenfrequencies in Fig. 5(b) (dotted curve) are not as well damped.

We continue by looking at the features of the position feedback and the family matrix, with the starting point from the dotted curves in Fig. 5. The magnitude difference of about 30 dB between the cases is suppressed by the family matrix, shown as the dashed curves in Fig. 6. Also, the low-frequency eigenmodes still present in the high spatial frequency case are attenuated. However, while the low and high spatial frequencies now have similar static gain, the low spatial frequency resonances are below the desired AO bandwidth. This is corrected by adding stiffness through the position feedback. To illustrate the effect of the position feedback clearly, the dotted curves in Fig. 6 show the closed-loop performance with ideal sensors. The dynamic behavior is now similar for both cases. Finally, the solid curves include the effect of the nonideal sensors. The roll off behavior of the sensors below 20 Hz gives rise to low-frequency asymptotes in the closed-loop response. The solid curves show the dynamical behavior of the DM system.

One final detail is that the piston is unobservable by the WFS in an AO system, and some piston control is needed to alleviate unnecessary stress that can slowly build up at the fixed inner rim of the DM. A better solution than driving the piston to zero is to subtract the mean force of the actuators closest to the rim from the displacement command at every location with some small gain; this additional feedback loop is shown in Fig. 4.

3. Adaptive Optics Control System

With the control architecture for the inner loop of the DM described in Section 2, we now introduce the outer AO loop, including wavefront sensing. The dynamic response of the DM system, shown as the solid lines in Fig. 6, is not the same as that of a

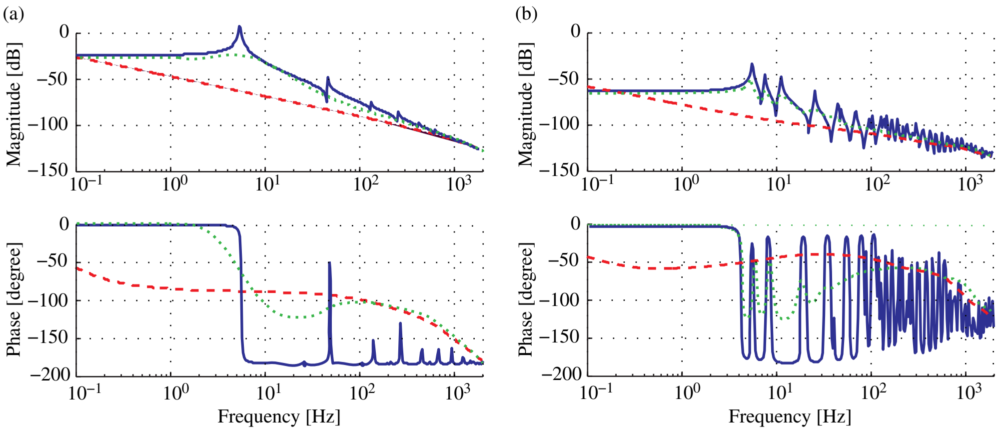

Fig. 5. (Color online) Transfer functions for (a) Case 1 (global), and (b) Case 2 (local). See text for case descriptions. The solid line shows the faceplate dynamics when $\mathbf{K}_v$ and $\mathbf{K}_p$ are null matrices and $\mathbf{Q}$ is an identity matrix. The dashed line illustrates the same situation, however with closed rate feedback, $\mathbf{K}_v$, and ideal sensors, whereas the dotted curve is for nonideal sensors. The conclusion is that the back sensors do not need to have bandwidth down to zero frequency.

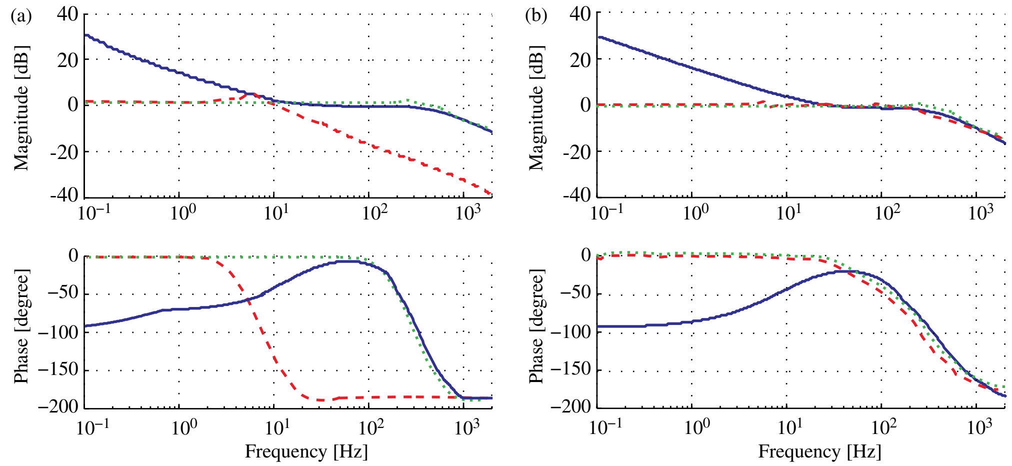

Fig. 6. (Color online) Frequency responses for (a) Case 1 (global), and (b) Case 2 (local). The dashed curves show the effect of the family matrix. The magnitude difference (seen in Fig. 5) is no longer present. The dotted curves show the dynamical behavior of the faceplate when the position feedback is closed with ideal sensors. The low-order eigenmodes are shifted toward higher frequencies, and the dynamical behavior is similar for the two cases. The solid curves show the frequency responses when nonideal sensors are used. The controlled DM has similar dynamic behavior for different spatial frequencies.

typical DM, but we demonstrate that it is sufficient for the purpose. The feedback control used for the AO system is shown in Fig. 7, where the plant is the DM system with the closed position and rate feedback loops as described above and shown in Fig. 4, and the input is the commanded displacement. The AO loop is closed with integral control, represented by the $\mathbf{K}_{\mathrm{AO}}/s$ block in Fig. 7.

The WFS-block in Fig. 7 is a matrix representing a Shack–Hartmann WFS with a square 22 × 22 lenslet array. The lenslet array is aligned such that the corners of the grid coincide with the actuator locations; see Fig. 8. Since the lenslet array map is larger than the DM, a mask is used to remove 88 subapertures. The four subapertures in the center are omitted because a pure piston displacement of the DM would give a nonzero WFS reading for the four subapertures in the center due to the inner boundary conditions. The tip and tilt for each remaining subaperture are computed from the wavefront samples at the actuator locations [9]

$$\mathrm{tip} = \frac{w(\mathbf{p}_1) + w(\mathbf{p}_2) - w(\mathbf{p}_3) - w(\mathbf{p}_4)}{2},$$

$$\mathrm{tilt} = \frac{w(\mathbf{p}_1) + w(\mathbf{p}_3) - w(\mathbf{p}_2) - w(\mathbf{p}_4)}{2},$$

where the two-dimensional vectors $\mathbf{p}_1$, $\mathbf{p}_2$, $\mathbf{p}_3$, and $\mathbf{p}_4$ define the locations of the four corner points of a subaperture, and $w(\mathbf{p})$ is the displacement.

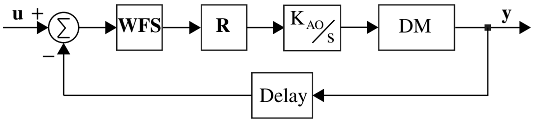

Fig. 7. Block diagram of the AO loop. The loop is closed with an integral controller.

The R-block in Fig. 7 is the reconstructor matrix, which is used for computation of DM actuator commands from the tip and tilt values of the WFS-matrix. The reconstructor is assembled using singular value decomposition of the interaction matrix, i.e., the matrix that describes the tip and tilt of the wavefront over the subapertures, when poking each DM actuator individually.

The performance of the AO loop is limited by the phase lag introduced by wavefront sampling and represented by the delay block in the control loop in Fig. 7. The delay is modeled as a fifth-order Padé approximation of e^{-sT}, where T is the delay time. Half the delay is from the WFS sampling period, and half is from the zero-order hold. The closed-loop performance and the rejection plot of the system in Fig. 7,

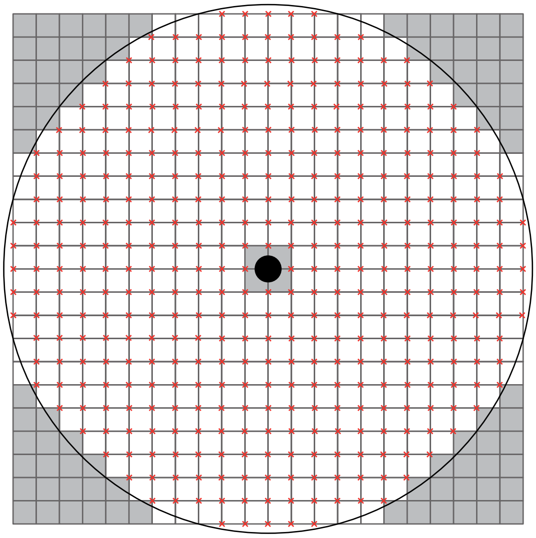

Fig. 8. (Color online) The lenslet array grid over the DM. Lenslets that are not completely filled by the light beam are not taken into account. Actuator locations are marked by crosses.

Table 2. The Parameters of the Atmosphere for $\lambda = 2200$ nm at La Palma [10]

Layer	Fried's parameter	Wind speed
1	1.48	12 m/s
2	4.21	18.6 m/s
3	6.96	8 m/s

from ϕ_{in} to ϕ_{res} at a representative location, is seen in Fig. 9 for $T = 1$ ms. The two cases (described in Subsection 2.C) represent the lowest and highest spatial frequencies that the DM can achieve. The difference between our DM system and an idealized DM (with a uniform behavior for all spatial frequencies and a flat frequency response) include the small difference between the spatial frequencies, an increase in low-frequency gain, and some additional phase lag at higher frequencies. The latter would become a significant factor for desired AO bandwidths above 100 Hz.

4. Influence of Atmosphere

Our proposed large DM concept, described in Sections 2 and 3, is studied in closed-loop AO operation. As an example for our study, we assume that the DM already introduced is the secondary in a two-mirror, 30 m telescope with AO. The observing wavelength is assumed to be 2200 nm. A three-layer atmosphere model is used with parameters taken from a study of the atmosphere over the La Palma observatory [10], as given in Table 2. The altitudes of the atmospheric layers are not of importance, since only objects at zenith are considered and the field is small. There are 20 actuators across the DM with an actuator pitch of 45 mm; thus the actuator pitch matches the Fried parameter of the first atmospheric layer.

A thin-layer model of the atmosphere is used with near-field propagation. Assuming Kolmogorov turbulence, the two-dimensional power spectrum of the phase is given by [9]

$$P_{\mathrm{atm}}(\rightarrow f) = \frac{0.0229}{r_0^{5/3} f^{11/3}}, \tag{4}$$

where r_0 is the Fried parameter and f is the magnitude of the spatial frequency vector $\rightarrow f$.

We now evaluate the AO performance in both the temporal and the frequency domain.

A. Performance for Different Zernike Polynomials

The AO system is null-seeking, and it is the task of the system to suppress input disturbance from the atmosphere to the extent possible. It is useful to expand the atmospheric phase into a series of Zernike polynomials. The power spectra for the individual Zernike polynomials, $P(\rightarrow f)$, can be computed from the power spectrum of the atmospheric turbulence as [11]

$$P(\rightarrow f) = |M(\rightarrow f)|^2 P_{\mathrm{atm}}(\rightarrow f), \tag{5}$$

where $M(\rightarrow f)$ is the Fourier transform of a specific Zernike polynomial. The Fourier transform of the Zernike polynomials is given by [12]

$$|M(\rightarrow f)| = \sqrt{n+1}\,\frac{2|J_{n+1}(\pi D_{\mathrm{DM}} f)|}{\pi D_{\mathrm{DM}} f} \times \begin{cases} \sqrt{2}|\cos(m\theta)| & \text{for } m \neq 0, \\ \sqrt{2}|\sin(m\theta)| & \text{for } m \neq 0, \\ 1 & m = 0, \end{cases}$$

where n is the radial degree, m is the azimuthal frequency of the polynomial, D_{DM} is the diameter of the DM, and $J_k(x)$ is the Bessel function of the first kind of the order k. Assuming frozen turbulence approximation (i.e., the phase screen shape remains unchanged when translated at the wind velocity V), the spatial power spectrum can be related to the temporal power spectrum as [11]

$$W(\nu) = \frac{1}{V}\int_{-\infty}^{+\infty} P\left(\frac{\nu}{V}, f_y\right) \mathrm{d}f_y.$$

Here, $\nu = V f_x$ is the temporal frequency. Using Eqs. (4) and (5), the temporal power spectrum related to a specific Zernike component at the DM is given by

$$W_{\mathrm{in}}(\nu) = \frac{0.0299}{V_{\mathrm{DM}} r_{0,\mathrm{DM}}^{5/3}} \int_{-\infty}^{+\infty} \left(\left(\frac{\nu}{V_{\mathrm{DM}}}\right)^2 + f_y^2\right)^{-11/6} \times \left|M\left(\frac{\nu}{V_{\mathrm{DM}}}, f_y\right)\right|^2 \mathrm{d}f_y, \tag{6}$$

where the wind speed and Fried's parameter have been scaled to the deformable secondary mirror. For our test case, the diameter of the telescope entrance pupil is 30 m, and the diameter of the DM is 1 m, so the scaling becomes $r_{0,\mathrm{DM}} = \frac{1}{30} r_0$ and $V_{\mathrm{DM}} = \frac{1}{30} V$.

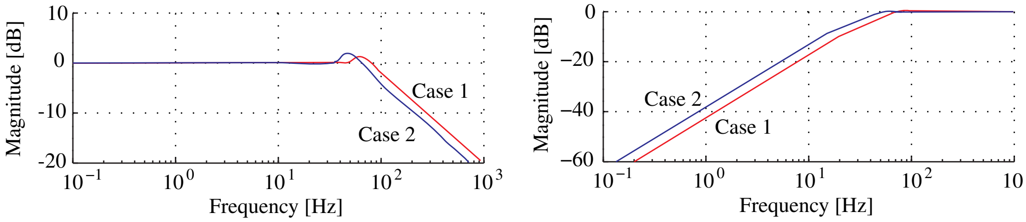

Fig. 9. (Color online) The closed-loop frequency response (to the left) and the rejection plot (to the right) of the system shown in Fig. 7, from ϕ_{in} to ϕ_{res} for a representative location. The two cases represent the lowest and highest spatial frequencies that the DM can achieve.

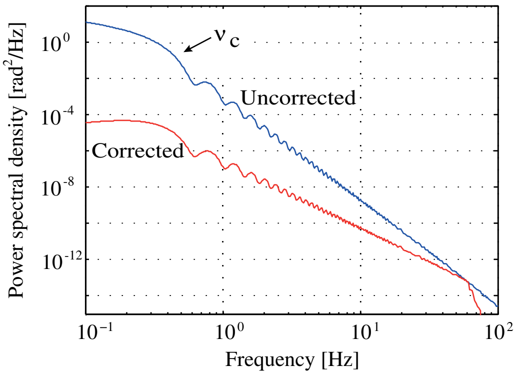

Fig. 10. (Color online) Temporal power spectra of the uncorrected and the corrected tilt term.

Note that only the first layer of the atmosphere in Table 2 is considered here.

The full AO system, described in Sections 2 and 3, is null-seeking. The disturbance for each Zernike polynomial is given by Eq. (6). The residual power spectrum is

$$W_{\text{out}}(\nu) = |H(\nu)|^2 W_{\text{in}}(\nu),$$

where $H(\nu)$ is the system rejection transfer function, shown in Fig. 9. The power spectra for the uncorrected and the corrected tilt mode of the atmosphere are shown in Fig. 10. The Zernike spectra are characterized by a cutoff frequency [11]

$$\nu_c = 0.3(n+1)\frac{V}{D},$$

where n is the radial order of the Zernike component.

The areas under the power spectra in Fig. 10 give the variance of the phase. The contribution of each Zernike mode can then be computed, and the result is shown in Fig. 11(a). The rms value of the wavefront for the first 25 Zernike modes is normalized with respect to the uncorrected tilt mode. The suppression of the Zernike modes, i.e., the residual divided by the input disturbances, is shown in Fig. 11(b).

The mean-square error for Kolmogorov turbulence is described by Noll [12] as $\sigma^2 = 1.0299(D/r_o)^{5/3}$. The mean-square residuals are suppressed by a factor of about 700 (rms reduction of 26). Thus, using Maréchal's approximation, the Strehl ratio is 0.8 for our case.

B. Time-Domain Simulation

A time-domain simulation of the full system, shown in Fig. 7, with an atmosphere model as input, ϕ_{in}, is used to demonstrate feasibility. The atmospheric disturbance model used is the three-layered atmosphere given in Table 2. The phase contributions from the different layers are assumed uncorrelated, and the net phase is the sum over the three layers, with frozen turbulence assumed. The layers obey Kolmogorov statistics given by Eq. (4).

A phase screen describes the phase difference added to a wavefront, when passing through a thin turbulent layer. Linear propagation through the screen is assumed; i.e., refraction is neglected. A phase screen, $\varphi(\mathbf{r})$, is composed by filtering a random function, $J(f)$, with the square root of the power spectrum of the two-dimensional phase, $W_{\text{in}}(f)$,

$$\varphi(\mathbf{r}) = \mathcal{F}^{-1}\left(\sqrt{W_{\text{in}}(f)}J(f)\right), \tag{7}$$

which is a method introduced by McGlamery [13].

A fourth-order Runge–Kutta method is used with a fixed integration interval of 50 μs. The sampling periods of the phase screens and the WFS are 1 ms and 2 ms, respectively. Linear interpolation is used to update the phase screen during a sampling period.

A result from a 3 s simulation is shown in Fig. 12. The two zooms show, respectively, the initial transient response of the mirror when it is commanded

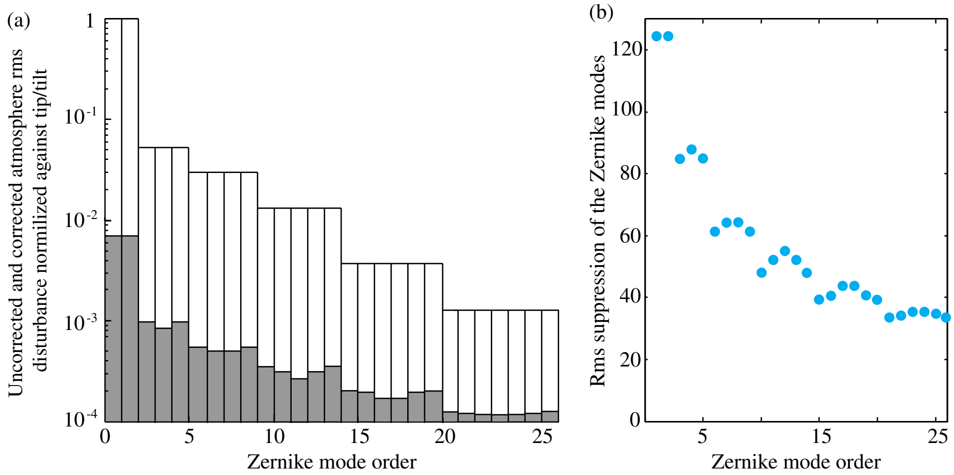

Fig. 11. (Color online) (a) Contribution of each Zernike mode to the uncorrected and corrected atmospheric rms disturbance normalized with respect to the tip/tilt mode before correction; empty bars refer to the uncorrected case, whereas filled bars refer to the corrected case. (b) Suppression factors for the rms wavefront errors of the lowest 25 Zernike components of the atmospheric phase noise.

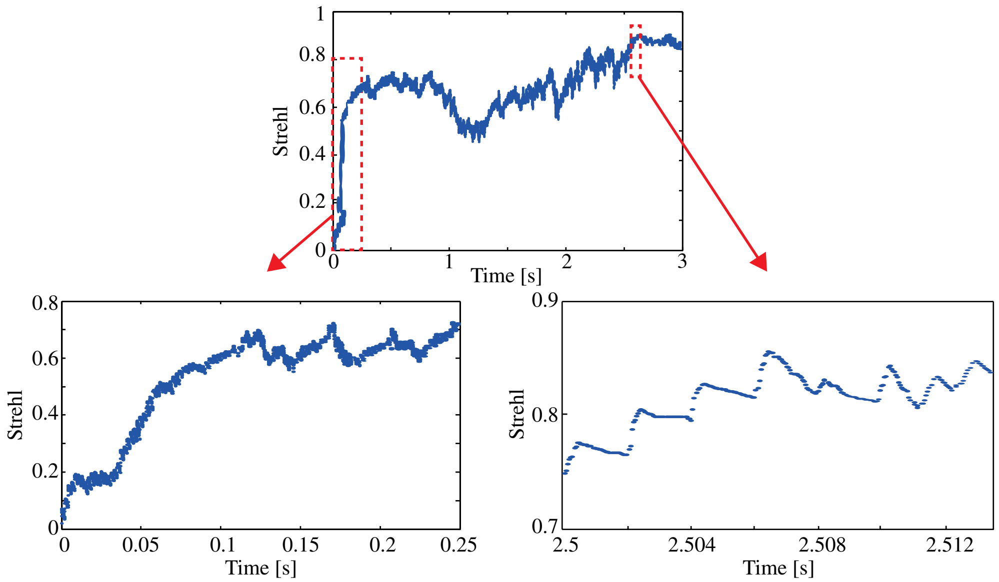

Fig. 12. (Color online) A three second time-domain simulation, where the Strehl ratio is computed for each time point. The zoom windows show the startup transient of the system from its rest position and a representative operation time interval, respectively.

from its rest position and a 14 ms window illustrating the typical behavior of the mirror during operation. The Strehl ratio is computed using Maréchal's approximation for all nodes across the mirror. If the performance during the startup transient is not considered, the average Strehl ratio is 0.77. The startup transient has a duration of 0.1 s due to actuator saturation. Further, the effect of temporal WFS sampling is apparent in the right zoom of Fig. 12. If our DM is replaced by an ideal DM, the average Strehl ratio is increased to 0.81 for the same phase screen. Thus, the main reducing factor of the AO system is the phase lag introduced by the AO loop.

5. Conclusions

We have demonstrated feasibility of a low-cost concept for a large DM for AO. Use of voice-coil (force) actuators results in a lightly-damped mirror with many structural modes within the AO control bandwidth, resulting in the need for feedback from electro-mechanical sensors to obtain dynamic response sufficient for AO. However, inexpensive electro-mechanical sensors can be used, because precision is not required quasi-statically, nor do the sensors need to be collocated with the actuators to provide active damping. The control system includes rate feedback to add damping, and a local family approach to suppress crosstalk between adjacent actuators. The latter ensures that the mirror has similar dynamic behavior for all the spatial frequencies that can be introduced by the actuators. Compared to an idealized DM, our concept will appear similarly inside an AO system for desired AO bandwidths of 100 Hz or below. If a higher AO bandwidth is required, the bandwidth of the actuators must be increased.

Performance prediction of the low-cost DM system has been simulated within an AO system. Atmospheric turbulence was included both using a Zernike polynomial expansion of the atmosphere and using a time-domain simulation showing the fluctuation of the Strehl ratio over time. The simulation, including a three-layer atmosphere, gave an average Strehl ratio of 0.77. This agrees well with the analytic approach, from which the Strehl ratio is determined to be 0.8.

With low-cost sensors and actuators, the dynamic behavior of the DM is not the same as that of a typical DM, but we have demonstrated that it provides good performance within an AO system. Compared to existing solutions, the suggested low-cost DM is made possible from the low electro-mechanical tolerances. The maintenance cost is also believed to be lower, because of the vacuum attachment concept.

References

1. J. Beckers, "NOAO proposal to NSF for 8 m telescopes," Appendix N, Tech. Rep., NOAO (1989).
2. B. Crepy, S. Chaillot, M. Cola, J. M. Conan, R. Cousty, M. Dimmler, J. L. Dournaux, S. De Zotti, E. Gabriel, R. Gasmi, R. Grasser, N. Hubin, P. Jagourel, L. Jochum, F. Locre, P.-Y. Madec, P. Morin, M. Mueller, G. Petit, D. Petitga, J. J. Roland, J. C. Sinquin, and E. Vernet, "Demonstration prototype and breadboards of the piezo stack M4 adaptive unit of the E-ELT," Proc. SPIE **7736**, 77365P (2010).
3. A. Riccardi, M. Xompero, D. Zanotti, L. Busoni, C. Del Vecchio, P. Salinari, P. Ranfagni, G. B. Zappellini, R. Biasi, M. Andrighettoni, D. Gallieni, E. Anaclerio, H. M. Martin, and M. S. Miller, "The adaptive secondary mirror for large binocular telescope: results of acceptance laboratory test," Proc. SPIE **7015**, 701512 (2008).
4. F. Quiros-Pacheco, L. Busoni, G. Aqapito, S. Esposito, E. Pinna, A. Puqlisi, and A. Riccardi, "First light AO (FLAO) system for LBT: performance analysis and optimization," Proc. SPIE **7736**, 773609 (2010).

5. T. Andersen, O. Garpinger, M. Owner-Petersen, F. Bjoorn, R. Svahn, and A. Ardeberg, “Novel concept for large deformable mirrors,” Opt. Eng. **45**, 073001 (2006).
6. D. G. MacMynowski, R. Heimsten, and T. Andersen, “Distributed force control of deformable mirrors,” Eur. J. Control **17**, 249–260 (2011).
7. H. M. Martin, G. B. Zappellini, B. Cuerden, S. M. Miller, A. Riccardi, and B. K. Smith, “Deformable secondary mirror for the LBT adaptive optics system,” Proc. SPIE **6272**, 672698 (2006).
8. R. Heimsten, M. Owner-Petersen, T. Ruppel, D. G. MacMynowski, and T. Andersen, “Suppressing low-order eigenmodes with local control for deformable mirrors,” Opt. Eng. (to be published).
9. J. W. Hardy, *Adaptive Optics for Astronomical Telescopes* (Oxford University, 1998).
10. C. Muoz-Tuon and J. Vernin, private communication.
11. J. M. Conan, G. Rousset, and P. Y. Madec, “Wave-front temporal spectra in high-resolution imaging through turbulence,” J. Opt. Soc. Am. A **12**, 1559–1570 (1995).
12. R. J. Noll, “Zernike polynomials and atmorspheric turbulence,” J. Opt. Soc. Am. **66**, 207–211 (1976).
13. B. L. McGlamery, “Computer simulation studies of compensation of turbulence degraded images,” Proc. SPIE **76**, 225 (1976).